

Explaining and Mitigating the Modality Gap in Contrastive Multimodal Learning

Can Yaras*, Siyi Chen*, Peng Wang, and Qing Qu

Department of Electrical Engineering & Computer Science,
University of Michigan

December 12, 2024

Abstract

Multimodal learning has recently gained significant popularity, demonstrating impressive performance across various zero-shot classification tasks and a range of perceptive and generative applications. Models such as Contrastive Language–Image Pretraining (CLIP) are designed to bridge different modalities, such as images and text, by learning a shared representation space through contrastive learning. Despite their success, the working mechanisms underlying multimodal learning are not yet well understood. Notably, these models often exhibit a *modality gap*, where different modalities occupy distinct regions within the shared representation space. In this work, we conduct an in-depth analysis of the emergence of modality gap by characterizing the gradient flow learning dynamics. Specifically, we identify the critical roles of mismatched data pairs and a learnable temperature parameter in causing and perpetuating the modality gap during training. Furthermore, our theoretical insights are validated through experiments on practical CLIP models. These findings provide principled guidance for mitigating the modality gap, including strategies such as appropriate temperature scheduling and modality swapping. Additionally, we demonstrate that closing the modality gap leads to improved performance on tasks such as image-text retrieval.

1 Introduction

Recently, significant progress has been made in multimodal learning, particularly in connecting text and image modalities through self-supervised methods that leverage large-scale paired data. These include image-text contrastive learning (Radford et al., 2021; Saharia et al., 2022a; Nichol et al., 2021), image-text matching (Li et al., 2021; Wang et al., 2022a; Li et al., 2022), and masked modeling (Li et al., 2021; Wang et al., 2022b,c). Following pre-training, shared conceptual representations enable a variety of downstream tasks, including text-to-image generation (Ramesh et al., 2021; Saharia et al., 2022a), image captioning (Wang et al., 2022c; Li et al., 2022), and vision-based question answering (Wang et al., 2022a; Dou et al., 2022). Among these, one of the most popular multimodal models is Contrastive Language–Image Pre-training (CLIP) (Radford et al., 2021), which effectively learns visual concepts from language supervision through contrastive learning. CLIP jointly trains a vision model and a language model by embedding a large corpus of image-text pairs into a shared embedding space using self-supervised learning. The training process employs

*The first two authors contributed to this work equally.

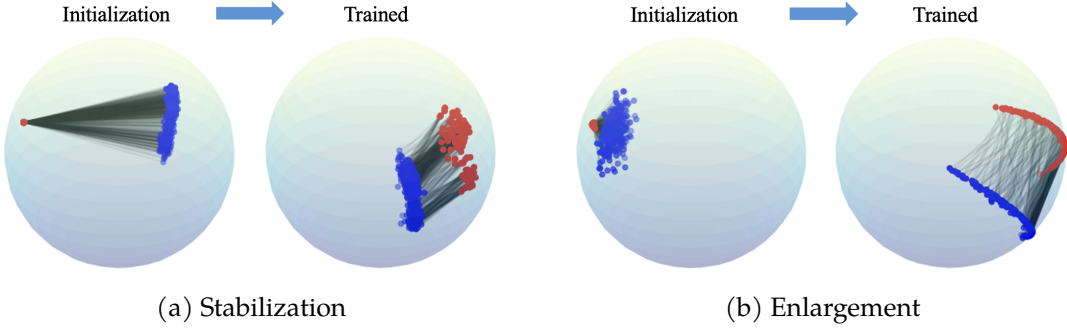


Figure 1: **Stabilization and enlargement of modality gap.** We visualize the CLIP text-image embedding space via PCA, where image features are in red and text features are in blue. A line connects each image-text pair. A modality gap emerges between image and text pairs. (a) After a long training, the gap between text and image still exists. (b) When two modalities are initialized with a small modality gap, the gap is still enlarged after training.

a contrastive learning objective (Chen et al., 2020), which encourages the model to bring similar pairs closer together in the embedding space, while it pushes dissimilar pairs further apart. The approach excels in zero-shot transfer for many downstream tasks across vision and language, even matching the performance of fully supervised models (Radford et al., 2021).

Despite their empirical success, a complete understanding of the mechanisms underlying multimodal learning models is lacking, with their behavior in certain scenarios even defying intuitive expectations about their design. For instance, while the contrastive loss is designed to align image embeddings with their corresponding text pairs, recent studies (Liang et al., 2022) have revealed a surprising phenomenon known as *modality gap*. As illustrated in Figure 1, this gap manifests as a significant separation between the embeddings of matched image-text pairs, with the two modalities occupying approximately parallel yet distant spaces (Zhang et al., 2022). Deepening our understanding of the factors underlying modality gap could shed light on the mechanisms driving the success of multimodal learning, as well as pave the way towards developing more effective multimodal models.

Prior arts & limitations. Driven by this goal, existing studies have investigated modality gap from a largely empirical perspective. However, a comprehensive and rigorous explanation of modality gap remains elusive. For example, Shi et al. (2023) empirically demonstrated that modality gap could be caused by the types of initialization and temperature scaling of the loss on simple datasets, but they fall short of providing theoretical justifications of their studies. Schrodi et al. (2024) investigated the role of imbalanced information between image and text modalities, implying that balancing the information complexity between text and image datasets could help mitigate modality gap. Again, their study is rather empirical without sufficient theoretical justifications. We postpone discussion of additional works and background on multimodal learning to Appendix A.

Understanding modality gap through learning dynamics. One surprising aspect of modality gap is that it contradicts with global optimality. Under ideal conditions, optimality conditions of the training loss imply perfect alignment between text and image embeddings. This is consistent with recent theoretical studies on neural collapse in classification problems (Papyan et al., 2020), which demonstrate that, with sufficiently large model capacity and perfect training, the classification head and the embeddings become perfectly aligned (Zhu et al., 2021; Yaras et al., 2022; Jiang et al., 2024; Wang et al., 2022d). Therefore, to gain deeper insight into the causes of modality gap, it is crucial to examine the factors influencing the learning dynamics of training these models. Moreover, empirical studies revealed several interesting phenomena in the learning dynamics, which

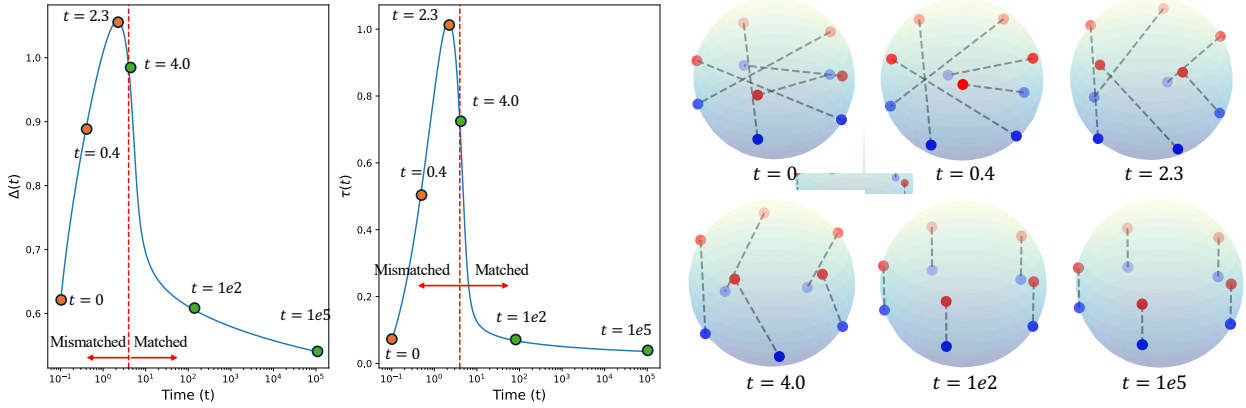


Figure 2: **Dynamics of modality gap Δ and temperature τ (defined in Section 2) during training on synthetic data.** Features from the two modalities are depicted in red and blue, with ground truth pairs connected by lines. At $t = 4.0$, all pairs are successfully matched. Initially, modality gap increases due to significant mismatches between pairs, but it decreases as the level of mismatch diminishes. Notably, modality gap and temperature exhibit highly coupled dynamics throughout the learning process.

could contribute to modality gap. Specifically, as shown by our experiments on both real datasets with practical networks (Figure 1) and synthetic datasets with simplified models (Figure 2), we observed the following when following the CLIP training procedure outlined by (Radford et al., 2021):

- **Enlargement of modality gap under mismatch.** When there exist mismatches¹ of image and text embeddings at initialization, modality gap between image and text enlarges as training progresses, as shown in Figure 1b. In particular, as shown in Figure 2, this usually happens in the early phase of training when we start from random initializations, where modality gap first increases and then decreases after pairs of image and text embeddings become better aligned.
- **Stabilization of modality gap due to learned temperature.** Furthermore, as shown by Liang et al. (2022), at random initialization, images and texts typically occupy distinct regions or “cones” within the feature space, resulting in a substantial modality gap. Observations in Figure 1a and Figure 2 imply that the gap-closing process remains limited when starting from random initialization. While the size of modality gap decreases in the later stages of training as mismatched pairs are reduced, it often stabilizes at a nonzero value, with limited reduction even as the training loss converges.

Summary of our contributions. In this work, we conduct a theoretical analysis of contrastive multimodal learning by examining the learning dynamics through the lens of gradient flow – a largely overlooked yet critical perspective for understanding the cause of modality gap. Our approach reveals the factors contributing to modality gap, explaining why it may stabilize at a certain level or even increase during training. Based on these insights, we propose theory-guided approaches to reduce the gap and improve downstream performance. Our key contributions are as follows:

- **Theoretical contributions.** Through a careful gradient flow analysis, we demonstrate that modality gap diminishes at the extremely slow rate of $\Omega(1/\log(t)^2)$ in training time t , explaining why modality gap is prevalent in multi-modal models such as CLIP. Our analysis highlights the role

¹For a pair $(\mathbf{h}_x, \mathbf{h}_y)$ of image and text embeddings, mismatch occurs if there exists an \mathbf{h}'_x such that \mathbf{h}'_x is “closer” to \mathbf{h}_y than \mathbf{h}_x (or the other way around)

of learned temperature in the persistence of modality gap, indicating several ways to reduce modality gap. Moreover, we rigorously demonstrate why and how modality gap can be created at initialization, suggesting that it cannot be simply closed before training.

- **Practical contributions.** Based on our theory, we propose practical methods, including temperature scheduling and exchanging features between modalities, to reduce modality gap and explore their benefits across several downstream tasks. We demonstrate that reducing the gap improves performance in image-text retrieval tasks but has a relatively smaller impact on visual classification including zero-shot and linear probing. In contrast, improving feature space uniformity proves to be more advantageous for visual classification tasks.

2 Problem Setup

In this section, we introduce the basic setup of the problem. We consider a set of n paired training samples $\{(\mathbf{x}_i, \mathbf{y}_i)\}_{i=1}^n \subseteq \mathbb{R}^{d_x} \times \mathbb{R}^{d_y}$. Here, $(\mathbf{x}_i, \mathbf{y}_i)$ denotes a pair of two data points from different modalities (such as image and text) that are considered to be related to each other, e.g., \mathbf{y}_i is the text caption of image \mathbf{x}_i . In multimodal learning, we want to align the image embedding $\mathbf{h}_{\theta, X}^i = f_{\theta}(\mathbf{x}_i)$ and the text embedding of $\mathbf{h}_{\phi, Y}^i = g_{\phi}(\mathbf{y}_i)$ through training two different deep networks $f_{\theta} : \mathbb{R}^{d_x} \rightarrow \mathbb{R}^d$ and $g_{\phi} : \mathbb{R}^{d_y} \rightarrow \mathbb{R}^d$ for each i .

Contrastive loss for multimodal learning. Let $\mathbf{H}_{\theta, X}, \mathbf{H}_{\phi, Y} \in \mathbb{R}^{n \times d}$ collectively denote the ℓ_2 -normalized embeddings of two different modalities:

$$\mathbf{H}_{\theta, X} = [\text{norm}(f_{\theta}(\mathbf{x}_1)) \ \dots \ \text{norm}(f_{\theta}(\mathbf{x}_n))]^\top, \quad \mathbf{H}_{\phi, Y} = [\text{norm}(g_{\phi}(\mathbf{y}_1)) \ \dots \ \text{norm}(g_{\phi}(\mathbf{y}_n))]^\top,$$

where the operator $\text{norm}(z) = z/\|z\|_2$ for any $z \in \mathbb{R}^d$. As shown in Radford et al. (2021), we can jointly learn the parameters θ, ϕ of networks f, g respectively via

$$\min_{\theta, \phi, \nu} \ell(\beta(\nu) \mathbf{H}_{\theta, X} \mathbf{H}_{\phi, Y}^\top) \quad (1)$$

where $\ell : \mathbb{R}^{n \times n} \rightarrow \mathbb{R}$ is a certain contrastive loss. Here, following the convention in Radford et al. (2021), $\beta(\cdot) : \mathbb{R} \rightarrow \mathbb{R}^+$ is the inverse temperature as a function of some learnable parameter ν , i.e., we have $\beta(\nu) = 1/\tau(\nu) = \exp(\nu)$ for training CLIP models where τ is the conventional temperature. Additionally, for ease of exposition, we drop the superscripts and just write $\mathbf{H}_X, \mathbf{H}_Y$.

The contrastive loss ℓ is determined solely by the pairwise (β -scaled) inner products between modalities. Its objective is to maximize the diagonal entries of $\beta \mathbf{H}_X \mathbf{H}_Y^\top$ while minimizing the off-diagonal elements. For instance, CLIP achieves this using a specific *symmetric* cross-entropy (CE) loss for ℓ , which we also adopt in this work. To derive this loss, we first define the standard (softmax) CE loss, $\ell_{\text{CE}}(\mathbf{m}, \mathbf{e}^{(i)})$, for logits $\mathbf{m} \in \mathbb{R}^n$ for a target one-hot distribution $\mathbf{e}^{(i)} \in \mathbb{R}^n$ as:

$$\ell_{\text{CE}}(\mathbf{m}, \mathbf{e}^{(i)}) := \log \left(\sum_{j=1}^n \exp(\mathbf{m}_j) \right) - \mathbf{m}_i.$$

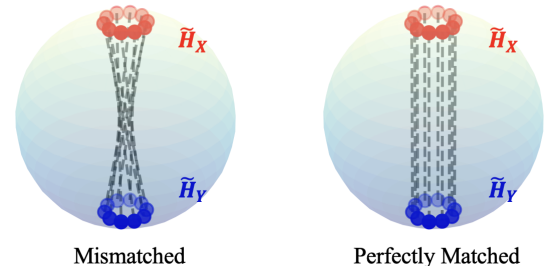


Figure 3: **Parallel modalities with or without mismatched pairs.** Ground truth pairs are connected by a dashed line.

Then, we can introduce ℓ as applying the usual CE loss to each row and column of \mathbf{M} individually and then averaging them:

$$\ell(\mathbf{M}) := \frac{1}{2n} \sum_{i=1}^n \left[\ell_{\text{CE}}(\mathbf{M}_{:,i}, \mathbf{e}^{(i)}) + \ell_{\text{CE}}(\mathbf{M}_{i,:}, \mathbf{e}^{(i)}) \right]. \quad (2)$$

Training loss with parallel embeddings. Motivated by recent empirical studies (Zhang et al., 2022), in this work we assume that the representations of each modality are *parallel*. Specifically, Zhang et al. (2022) has empirically discovered that *inter-modality* variance and *intra-modality* variance are found to be orthogonal. Mathematically, we can impose the parallel constraint by replacing \mathbf{H}_X with $\tilde{\mathbf{H}}_X = [\sqrt{1 - \gamma_X^2} \mathbf{H}_X \quad \gamma_X \mathbf{1}_n]$ and \mathbf{H}_Y with $\tilde{\mathbf{H}}_Y = [\sqrt{1 - \gamma_Y^2} \mathbf{H}_Y \quad \gamma_Y \mathbf{1}_n]$, where $\gamma_X, \gamma_Y \in [-1, 1]$. For simplicity, we assume that $\gamma_X = \gamma$ and $\gamma_Y = -\gamma$ for some $\gamma \in [-1, 1]$. Then, (1) becomes

$$\min_{\theta, \phi, \nu, \gamma} \ell(\beta(\nu) \tilde{\mathbf{H}}_X \tilde{\mathbf{H}}_Y^\top) = \ell(\beta(\nu)(1 - \gamma^2) \mathbf{H}_X \mathbf{H}_Y^\top). \quad (3)$$

Gradient flow dynamics. We consider the training dynamics of (3) under continuous-time gradient flow, i.e., for time $t \geq 0$, the quantities $\theta(t), \phi(t), \nu(t), \gamma(t)$ satisfy

$$\frac{d\theta(t)}{dt} = -\frac{\partial \ell}{\partial \theta}, \quad \frac{d\phi(t)}{dt} = -\frac{\partial \ell}{\partial \phi}, \quad \frac{d\nu(t)}{dt} = -\frac{\partial \ell}{\partial \nu}, \quad \frac{d\gamma(t)}{dt} = -\frac{\partial \ell}{\partial \gamma} \quad (4)$$

with initial conditions $\theta(0) = \theta_0$, $\phi(0) = \phi_0$, $\nu(0) = \nu_0$, and $\gamma(0) = \gamma_0$. We refer the reader to Appendix B.1 for the derivative and gradient computations.

Measures of modality gap and margin. Based on the above assumptions of parallel embeddings between two modalities, we introduce two metrics of modality gap and margin that will be useful in our analysis. Given the reparameterized embeddings $\tilde{\mathbf{H}}_X$ and $\tilde{\mathbf{H}}_Y$ of the image \mathbf{X} and text \mathbf{Y} that we introduced above, where each row $\tilde{\mathbf{h}}_x^i, \tilde{\mathbf{h}}_y^i$ of $\tilde{\mathbf{H}}_X, \tilde{\mathbf{H}}_Y$ respectively correspond to a data sample, we define the modality centers as

$$\mathbf{c}_X = \frac{1}{n} \sum_{j=1}^n \tilde{\mathbf{h}}_x^j, \quad \mathbf{c}_Y = \frac{1}{n} \sum_{j=1}^n \tilde{\mathbf{h}}_y^j.$$

Following Liang et al. (2022), we can measure the *modality gap* by the center distance between two modalities as

$$\Delta := \|\mathbf{c}_X - \mathbf{c}_Y\|.$$

As such, a larger center distance implies a larger modality gap. Moreover, the modality gap Δ also satisfies $\Delta \geq 2\gamma$, which will simplify our analysis in Section 3.

In our analysis, we also introduce a notion of *margin* to measure the match (angles) between associated pairs $(\mathbf{x}_i, \mathbf{y}_i)$ in the embedding space. Intuitively, we want to measure the matchness by measuring the correlation between \mathbf{x}_i and \mathbf{y}_i in the embedding space. Let $\mathbf{Z} = \mathbf{H}_X \mathbf{H}_Y^\top$, which compute the correlation between \mathbf{H}_X and \mathbf{H}_Y . We define the margin by

$$\alpha(\mathbf{Z}) := \min_{i \neq j} (\mathbf{Z}_{i,i} - \mathbf{Z}_{i,j}) \wedge (\mathbf{Z}_{j,j} - \mathbf{Z}_{i,j}),$$

where \wedge denotes minimum. Based on $\alpha(\mathbf{Z})$, we say that $\mathbf{H}_X, \mathbf{H}_Y$ are *perfectly matched* if $\alpha(\mathbf{H}_X \mathbf{H}_Y^\top) > 0$, otherwise we say that they are *mismatched*. An illustration of perfectly matched and mismatched data pairs is shown in Figure 3. Intuitively, perfectly matched means all ground truth pairs are the closest to each other.

3 Explaining the Modality Gap

In this section, we provide our main theoretical results that explain how modality gap emerges and remains throughout training.

3.1 Learning Temperature Stabilizes Modality Gap

As shown in Figure 2, modality gap $\Delta \geq 2\gamma$ and temperature τ are highly coupled, implying that learnable temperature plays a crucial role in the rate at which modality gap closes. Based upon the problem setup in Section 2, the following lemma directly reveals this relationship.

Lemma 3.1. *Let $\nu(t)$ and $\gamma(t)$ be solutions to the gradient flow dynamics given in (4). Then we have*

$$R = \frac{d\gamma/dt}{d\beta/dt} = -\frac{2\beta(\nu)\gamma}{\beta'(\nu)^2(1-\gamma^2)} \quad (5)$$

for all $t \geq 0$, where $\beta'(\nu)$ denotes the derivative of β with respect to ν . Moreover, given $\beta(\nu) = \exp(\nu)$, we have $\beta'(\nu) = \beta$ and the following holds:

$$\beta = \beta_0 \sqrt{\frac{\gamma_0}{\gamma}} \exp\left(\frac{\gamma^2 - \gamma_0^2}{4}\right), \quad \text{and} \quad R = \Theta(1/\beta). \quad (6)$$

The proof of Lemma 3.1 is provided in Appendix B.2. The lemma relates the rates at which γ and β change, while $R = \Theta(1/\beta)$ implies that the ratio R decays to zero as β grows to infinity. This implies that an increasing β will dominate the decrease in γ , preventing modality gap Δ from closing (i.e., its lower bound 2γ remains positive). This is made precise in the following theorem.

Theorem 3.2. *Based on the problem setup in Section 2, consider the gradient flow dynamics (4) for solving (3). Suppose $\mathbf{Z}(t) = \mathbf{H}_X(t)\mathbf{H}_Y^\top(t)$ and the initial temperature $\beta_0 \geq \log(4(n-1))/(\bar{\alpha}(1-\gamma_0^2))$ with $\beta(\nu) = \exp(\nu)$, and assume that the margin satisfies $\alpha(\mathbf{Z}(t)) \geq \bar{\alpha}$ for all $t \geq 0$ for some $\bar{\alpha} > 0$. Then modality gap Δ satisfies*

$$\Delta(t) \geq \Omega\left(\frac{1}{\log(t)^2}\right) \text{ for all } t \geq 0. \quad (7)$$

The proof can be found in Appendix B.3. To elaborate, consider the simplified setting where we replace ℓ in (3) with the scalar function $\ell(m) = \exp(-m)$ mimicking the exponential tail of the cross-entropy loss. The gradient flow in this case is simply given by $d\gamma/dt = -2\beta\gamma \exp(-\beta(1-\gamma^2))$, so via the equality (6) we have $d\gamma/dt = \Omega(-\gamma^{1/2} \exp(-c\gamma^{-1/2})) = \Omega(-\gamma^{3/2} \exp(-c'\gamma^{-1/2}))$, for some $c' < c$. Integrating this equation and applying the inequality $\Delta \geq 2\gamma$ yields $\Delta(t) \geq \Omega(1/\log(t)^2)$.

Remarks. We discuss Theorem 3.2 in the following:

- **Slow closure of modality gap.** The result in (7) indicates that Δ , with rate $\Omega(1/\log(t)^2)$, approaches zero exceedingly slowly. Consequently, this lower bound implies that closing modality gap would require an impractically long training time. As shown in Figure 4a, this can be verified in practice on CLIP models trained on the MSCOCO dataset. Specifically, we sample 2048 random pairs of data and train the model from scratch for 10000 steps and record modality gap during training. In Figure 4a, we report modality gap from the 100th step when the gap begins to decrease consistently. The modality gap $\Delta(t)$ versus $-1/\log(t)^2$ exhibits a linear relationship, verifying our result and slow closure.

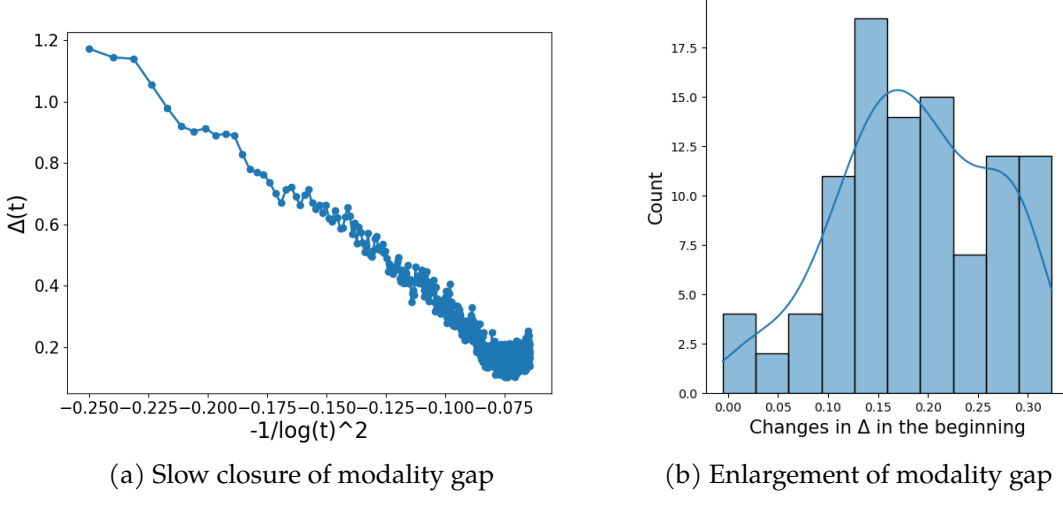


Figure 4: **Verifying theoretical results.** We sample 2048 random pairs of MSCOCO examples and utilize a standard CLIP model to (a) plot Δ throughout training from scratch and (b) plot a histogram of the change in Δ across 100 initializations in the first 10 steps of training. More details regarding the experimental setup can be found in Appendix E.

- **Discussion on the assumptions.** In Theorem 3.2, we assume a positive margin $\bar{\alpha} > 0$ throughout training, ensuring a minimum $\bar{\alpha}$ gap between perfectly matched and mismatched pairs. While primarily for analytical purposes, this assumption can be relaxed in practice, as shown in the early stage of Figure 4a, where the result holds even with many mismatched pairs. Additionally, while parallel embeddings between modalities are typically valid, breaking this constraint can help to mitigate modality gap, a strategy we leverage in Section 4. We also assume a sufficiently large initial inverse temperature β_0 , a common practice Radford et al. (2021). Crucially, the choice $\beta(\nu) = \exp(\nu)$ is essential for achieving the rate in Theorem 3.2; changing β or employing a temperature schedule (see Section 4) can significantly change the convergence rate of modality gap. For details on convergence rates with various schemes, see Appendix C. We evaluate these methods for reducing modality gap and their impact on downstream performance in Section 4.

3.2 Mismatched Pairs Enlarge Modality Gap at Early Training Stages

Second, we show that modality gap can be enlarged at the early stage of training, due to the large amount of mismatched pairs caused by random initialization. This further adds to the difficulty of closing modality gap.

Theorem 3.3. Suppose the rows of $\mathbf{H}_X(0), \mathbf{H}_Y(0)$ are drawn independently and uniformly from \mathbb{S}^{d-1} and let $a = \beta_0(1 - \gamma_0^2)$. Then with probability $1 - \delta$, we have

$$\frac{d\Delta}{dt} \Big|_{t=0} \geq 4\beta_0\gamma_0 \left(\frac{\xi_1 - 2e^a\epsilon}{\xi_2 + (e^a - e^{-a})\epsilon} - 2\epsilon \right) \quad (8)$$

where $\epsilon = \sqrt{\log((4n + 1)/\delta)/(2n)}$ and

$$\xi_1 = \Gamma\left(\frac{d}{2}\right) \left(\frac{2}{a}\right)^\rho \left(I_{\rho-1}(a) - \frac{2\rho}{a} I_\rho(a) \right), \quad \xi_2 = \Gamma\left(\frac{d}{2}\right) \left(\frac{2}{a}\right)^\rho I_\rho(a),$$

where $\rho = (d - 2)/2$, Γ is the gamma function, and $I_\rho(z)$ is the modified Bessel function of the first kind.

The proof of Theorem 3.3 is given in Appendix B.4. In addition to the parallel modalities assumption, we assume that embeddings are uniformly distributed on the hypersphere. This aligns

with practice, as the final-layer linear projections of f_θ and g_ϕ are typically initialized from a zero-mean isotropic Gaussian distribution, resulting in normalized features uniformly spread over the hypersphere. Next, we discuss Theorem 3.3 in the following:

- **Interpretation.** As the number of training samples n is very large in practice, we can analyze the form of (8) in the limit $n \rightarrow \infty$, which gives

$$\frac{d\Delta}{dt} \Big|_{t=0} \geq 4\beta_0\gamma_0 \frac{\xi_1}{\xi_2} = 4\beta_0\gamma_0 \left(\frac{I_{\rho-1}(a)}{I_\rho(a)} - \frac{2\rho}{a} \right) \quad (9)$$

almost surely. From the recurrence relation $I_{\rho-1}(a) = I_{\rho+1}(a) + (2\rho/a)I_\rho(a)$ in (Magnus et al., 1967, (3.1.1)) and the fact that $I_\rho(z) > 0$ for real order ρ and $z > 0$, we have

$$\frac{I_{\rho-1}(a)}{I_\rho(a)} - \frac{2\rho}{a} = \frac{I_{\rho+1}(a)}{I_\rho(a)} > 0$$

so $d\Delta/dt > 0$ at $t = 0$, i.e., modality gap enlarges initially. Moreover, we can write (9) in terms of elementary functions in the special case $d = 3$. From $\rho = 1/2$, we have

$$\frac{d\Delta}{dt} \Big|_{t=0} \geq 4\beta_0\gamma_0 \left(\frac{I_{-1/2}(a)}{I_{1/2}(a)} - \frac{1}{a} \right) = 4\beta_0\gamma_0 \left(\frac{\cosh(\beta_0(1 - \gamma_0^2))}{\sinh(\beta_0(1 - \gamma_0^2))} - \frac{1}{\beta_0(1 - \gamma_0^2)} \right)$$

from closed-form expressions for half odd integer order Bessel functions (Magnus et al., 1967, (3.3)). For $\gamma_0 = \Theta(1)$, this gives $d\Delta/dt \geq \Theta(\beta_0 \tanh(\beta_0)) \sim \beta_0$. As such, a large initial inverse temperature (which is used in practice) encourages a large increase in Δ at initialization.

- **Experimental verification.** We verify that $d\Delta/dt > 0$ at initialization as implied by Theorem 3.2 in practice via randomly initializing CLIP models and recording the change in modality gap after the first 10 steps. We measure the change in modality gap with 100 independent trials and present the distribution of changes in Figure 4b. From Figure 4b, we can see modality gap increases at the start of training for all random initialization, with the mean being near 0.15.

4 Mitigating the Modality Gap

The analysis of learning dynamics in Section 3 offers valuable insights into mitigating modality gap. It inspires us to design two types of methods for reducing modality gap: (i) **Temperature Control**, where we propose new temperature scheduling rules for accelerating the convergence rate of modality gap, and (ii) **Modality Swapping**, we proposed methods to manually break the parallel constraints of two modalities by swapping them during training. To evaluate these approaches, we train models from scratch on the MSCOCO dataset with different variants of the proposed methods and then measure modality gap and evaluate the performance on downstream tasks. In the following, we introduce the proposed methods in Section 4.1 and discuss the results and implications of reducing modality gap in Section 4.2.

4.1 Methods

We introduce the main idea of each method, and leave details on implementations to Appendix D.

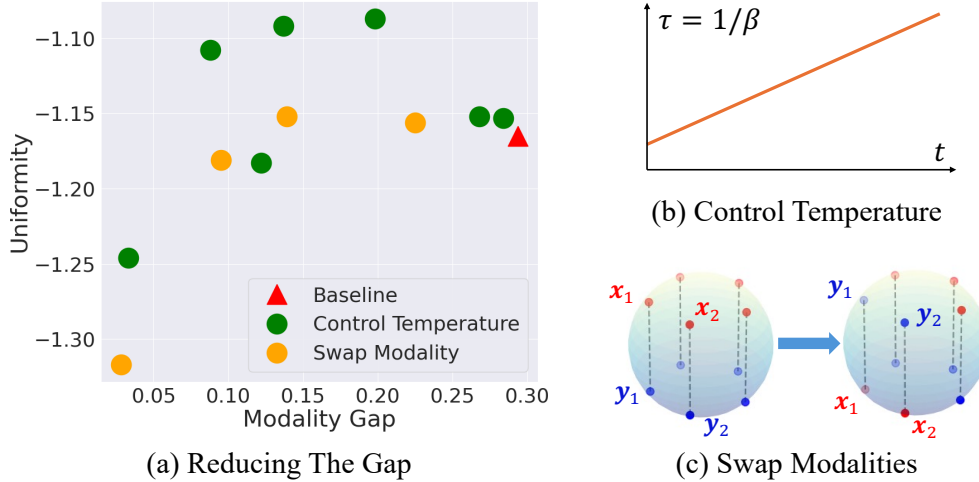


Figure 5: **We propose two categories of methods: Control Temperature and Swap Modality.** (a) Our methods reduce modality gap and may influence the uniformity of the feature space. (b) **Control Temperature** maintains the temperature at larger values such as increasing temperature across training. (c) **Swap Modalities** swaps between image and text feature pairs.

Temperature Control. Our first type of method involves the control of temperature $\tau(\nu)$ during training. As defined in (1), $\beta(\nu) = 1/\tau(\nu) = \exp(\nu)$ is the temperature parameterization. Usually, $\tau(\nu)$ is the so-called *temperature* in CLIP loss Chen et al. (2020); Radford et al. (2021). Thus, we refer to $\tau(\nu)$ as *temperature* when we introduce the following methods. As implied by analysis in Section 3.1 and Appendix C, we can control the temperature $\tau(\nu)$ to accelerate the rate at which modality gap closes – we propose the following variants to achieve this:

- Temperature Scheduling (TS): Instead of allowing $\tau(\nu)$ to diminish freely with ν (as shown in Figure 5(b)), we enforce a linearly increasing schedule for τ during training.
- Temperature Reparameterization (TR): As mentioned in Section 3.1, the specific parameterization of temperature also affects the gap closing rate. We replace the original parameterization, $1/\tau(\nu) = \beta(\nu) = \exp(\nu)$, with alternatives that yield a higher gap closing rate, such as $1/\tau(\nu) = \log(1 + e^\nu)$.
- Smaller Learning Rate of Temperature (SLRT): We use a smaller learning rate for the temperature parameter compared to other learnable parameters. This slows down the decrease in temperature, allowing larger temperature values to be maintained during training.
- Fixed on Large Temperature (FLT): Rather than allowing the temperature to be freely learned, we fix τ at a high value throughout the training process.

Modality Swapping. Our second approach involves manually mixing the two modalities by swapping pairs, as illustrated in Figure 5c. This mixing prevents the two modalities from remaining segregated into parallel planes. Consequently, the repulsion caused by mismatched pairs no longer occurs between the original planes, thereby reducing the overall repulsion between them. We introduce two strategies for swapping pairs—hard swapping and soft swapping—both of which effectively mitigate modality gap.

- Hard Swapping Between Modalities (HS). During training, we randomly select some images and their paired text descriptions. Then, we exchange the features of these images and the paired texts in the shared feature space, as visualized in Figure 5c.

- Soft Swapping Between Modalities (SS). Different from hard swapping, for a pair of image and text features, soft swapping mixes the two features to create a pair of image and text features.

4.2 Experimental Results and Implications

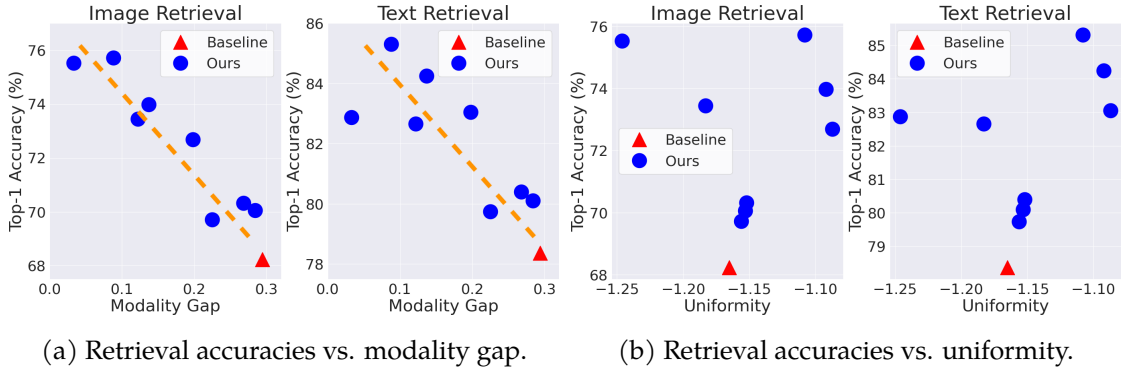


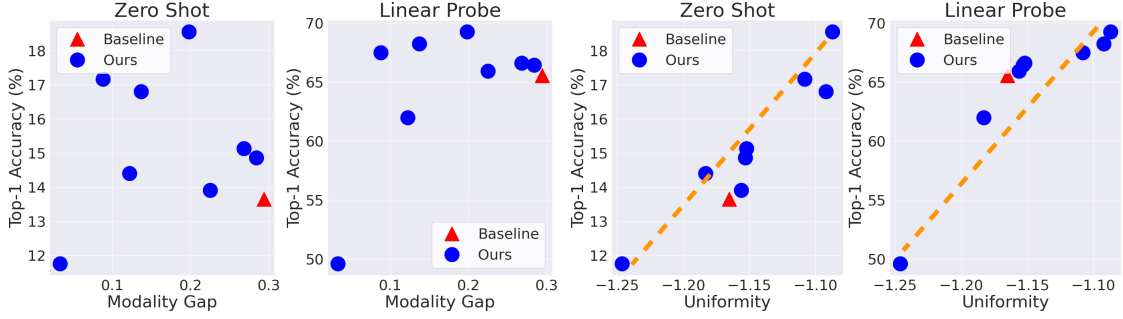
Figure 6: **Image-text retrieval accuracy increases with reduced modality gap by our proposed methods.** Uniformity does not show strong correlations with retrieval accuracies.

Experimental setup. We train CLIP models from scratch on MSCOCO using the proposed methods and the original CLIP training process as a baseline. After pretraining, we evaluate two key attributes of the shared feature space: (i) modality gap between image and text features and (ii) feature space uniformity. Additionally, we assess the models on four downstream tasks: (i) zero-shot image classification, (ii) linear-probe image classification, (iii) image-text retrieval, and (iv) vision-language question answering (MMVP-VLM Tong et al. (2024)). For each training setting, we independently train three models and report averaged results for attributes and task performance. Detailed experimental setup is provided in Appendix E.

Closing modality gap is especially helpful for image-text retrievals. We visualize the correlation between image-text retrieval accuracies and modality gap in Figure 6a, and the correlation between image-text retrieval accuracies and uniformity in Figure 6b. As shown in the figure, though these methods are different variants of Control Temperature and Swap Modality, a smaller modality gap clearly leads to a higher retrieval accuracy. This indicates reducing modality gap improves image-text retrieval. In contrast, uniformity does not show a strong correlation with the retrieval accuracy. We include more detailed results for each method variant in Appendix F.

	Baseline	FLT			TS		
		$4 \cdot 10^{-2}$	$7 \cdot 10^{-2}$	10^{-1}	S1	S2	S3
Modality Gap (\downarrow)	0.294	0.122	0.033	0.019	0.198	0.137	0.088
Uniformity (\uparrow)	-1.165	-1.183	-1.246	-1.251	-1.087	-1.092	-1.108
MMVP-VLM (\uparrow)	14.321	11.852	14.074	14.817	14.074	14.321	13.087

Table 1: **MMVP-VLM accuracy does not strongly correlate with modality gap or uniformity.**



(a) Zero shot/linear probe vs. modality gap. (b) Zero shot/linear probe vs. uniformity.

Figure 7: **Zero-shot and linear probe accuracies are not strongly correlated with modality gap.** Uniformity has a clear positive correlation with zero-shot and linear probe accuracies instead.

Closing modality gap is not all you need. Even though methods reducing modality gap increase retrieval performance, it does not mean modality gap is the only metric we should care about when characterizing the space. For example, as shown in Figure 7, bad uniformity will harm zero-shot and linear probe accuracies while a reduced modality gap does not have an obvious effect on them. Moreover, for the difficult vision-language question-answering task MMVP-VLM, we test different variants of Fixed on Large Temperature (FLT) and Temperature Scheduling (TS), and neither modality gap nor uniformity shows a strong correlation with the MMVP-VLM performance. We discuss the detailed settings of different variants in Appendix D and Appendix F

5 Conclusion

In this work, we investigated the modality gap in training multimodal models. By analyzing gradient flow learning dynamics, we theoretically characterized how learning temperature and mismatched pairs influence this gap. Based on our analysis, we proposed principled methods to control temperature and swap information between modalities to reduce the gap, which also improves downstream task performance—particularly in retrieval tasks. Our work opens up future directions, such as extending gradient flow analysis to study the difficulty of closing the gap with varying levels of shared information between modalities by modeling data distributions. Additionally, our results can provide insights into finetuning scenarios where domain differences between pretraining and finetuning data need to be considered. Motivated by recent advancements in understanding the compressibility of gradient dynamics through low-dimensional structures in data (Yaras et al., 2023, 2024; Kwon et al., 2024), a promising future direction is to investigate the compressibility of the Riemannian dynamics trajectory in multimodal learning to enhance the efficiency and performance of multimodal models.

Acknowledgment

We acknowledge support from NSF CAREER CCF-2143904, NSF IIS 2312842, NSF IIS 2402950, and ONR N00014-22-1-2529. Additionally, we acknowledge fruitful discussions with Yuexiang Zhai (UC Berkeley) and Liyue Shen (UMich).

References

Alec Radford, Jong Wook Kim, Chris Hallacy, Aditya Ramesh, Gabriel Goh, Sandhini Agarwal, Girish Sastry, Amanda Askell, Pamela Mishkin, Jack Clark, et al. Learning transferable visual models from natural language supervision. In *International conference on machine learning*, pages 8748–8763. PMLR, 2021.

Chitwan Saharia, William Chan, Saurabh Saxena, Lala Li, Jay Whang, Emily Denton, Seyed Kamalar Seyed Ghasemipour, Burcu Karagol Ayan, S Sara Mahdavi, Rapha Gontijo Lopes, Tim Salimans, Jonathan Ho, David J Fleet, and Mohammad Norouzi. Photorealistic text-to-image diffusion models with deep language understanding. *arXiv preprint arXiv:2205.11487*, 2022a.

Alex Nichol, Prafulla Dhariwal, Aditya Ramesh, Pranav Shyam, Pamela Mishkin, Bob McGrew, Ilya Sutskever, and Mark Chen. Glide: Towards photorealistic image generation and editing with text-guided diffusion models. *arXiv preprint arXiv:2112.10741*, 2021.

Junnan Li, Ramprasaath Selvaraju, Akhilesh Gotmare, Shafiq Joty, Caiming Xiong, and Steven Chu Hong Hoi. Align before fuse: Vision and language representation learning with momentum distillation. *Advances in neural information processing systems*, 34:9694–9705, 2021.

Peng Wang, An Yang, Rui Men, Junyang Lin, Shuai Bai, Zhikang Li, Jianxin Ma, Chang Zhou, Jingen Zhou, and Hongxia Yang. Ofa: Unifying architectures, tasks, and modalities through a simple sequence-to-sequence learning framework. In *International Conference on Machine Learning*, pages 23318–23340. PMLR, 2022a.

Junnan Li, Dongxu Li, Caiming Xiong, and Steven Hoi. Blip: Bootstrapping language-image pre-training for unified vision-language understanding and generation. *arXiv preprint arXiv:2201.12086*, 2022.

Wenhui Wang, Hangbo Bao, Li Dong, Johan Bjorck, Zhiliang Peng, Qiang Liu, Kriti Aggarwal, Owais Khan Mohammed, Saksham Singhal, Subhajit Som, and Furu Wei. Image as a foreign language: Beit pretraining for all vision and vision-language tasks. *arXiv preprint arXiv:2208.10442*, 2022b.

Jianfeng Wang, Zhengyuan Yang, Xiaowei Hu, Linjie Li, Kevin Lin, Zhe Gan, Zicheng Liu, Ce Liu, and Lijuan Wang. Git: A generative image-to-text transformer for vision and language. *arXiv preprint arXiv:2205.14100*, 2022c.

Aditya Ramesh, Mikhail Pavlov, Gabriel Goh, Scott Gray, Chelsea Voss, Alec Radford, Mark Chen, and Ilya Sutskever. Zero-shot text-to-image generation. In *International Conference on Machine Learning*, pages 8821–8831. PMLR, 2021.

Zi-Yi Dou, Yichong Xu, Zhe Gan, Jianfeng Wang, Shuohang Wang, Lijuan Wang, Chenguang Zhu, Pengchuan Zhang, Lu Yuan, Nanyun Peng, Zicheng Liu, and Michael Zeng. An empirical study of training end-to-end vision-and-language transformers. In *Proceedings of the IEEE/CVF Conference on Computer Vision and Pattern Recognition*, pages 18166–18176, 2022.

Ting Chen, Simon Kornblith, Mohammad Norouzi, and Geoffrey Hinton. A simple framework for contrastive learning of visual representations. In Hal Daumé III and Aarti Singh, editors, *International Conference on Machine Learning (ICML)*, volume 119 of *Proceedings of Machine Learning Research*, pages 1597–1607. PMLR, 2020. URL <https://proceedings.mlr.press/v119/chen20j.html>.

Victor Weixin Liang, Yuhui Zhang, Yongchan Kwon, Serena Yeung, and James Y Zou. Mind the gap: Understanding the modality gap in multi-modal contrastive representation learning. *Advances in Neural Information Processing Systems*, 35:17612–17625, 2022.

Yuhui Zhang, Jeff Z HaoChen, Shih-Cheng Huang, Kuan-Chieh Wang, James Zou, and Serena Yeung. Diagnosing and rectifying vision models using language. In *The Eleventh International Conference on Learning Representations*, 2022.

Peiyang Shi, Michael C. Welle, Mårten Björkman, and Danica Kragic. Towards understanding the modality gap in CLIP. In *ICLR 2023 Workshop on Multimodal Representation Learning: Perks and Pitfalls*, 2023. URL <https://openreview.net/forum?id=8W3KGzw7fNI>.

Simon Schrodi, David T. Hoffmann, Max Argus, Volker Fischer, and Thomas Brox. Two effects, one trigger: On the modality gap, object bias, and information imbalance in contrastive vision-language representation learning, 2024. URL <https://arxiv.org/abs/2404.07983>.

Vardan Papyan, XY Han, and David L Donoho. Prevalence of neural collapse during the terminal phase of deep learning training. *Proceedings of the National Academy of Sciences*, 117(40):24652–24663, 2020.

Zhihui Zhu, Tianyu Ding, Jinxin Zhou, Xiao Li, Chong You, Jeremias Sulam, and Qing Qu. A geometric analysis of neural collapse with unconstrained features. *Advances in Neural Information Processing Systems*, 34:29820–29834, 2021.

Can Yaras, Peng Wang, Zhihui Zhu, Laura Balzano, and Qing Qu. Neural collapse with normalized features: A geometric analysis over the riemannian manifold. *Advances in neural information processing systems*, 35:11547–11560, 2022.

Jiachen Jiang, Jinxin Zhou, Peng Wang, Qing Qu, Dustin G. Mixon, Chong You, and Zhihui Zhu. Generalized neural collapse for a large number of classes. In *Proceedings of the 41st International Conference on Machine Learning*, volume 235 of *Proceedings of Machine Learning Research*, pages 22010–22041. PMLR, 2024.

Peng Wang, Huikang Liu, Can Yaras, Laura Balzano, and Qing Qu. Linear convergence analysis of neural collapse with unconstrained features. In *OPT 2022: Optimization for Machine Learning (NeurIPS 2022 Workshop)*, 2022d.

Wilhelm Magnus, Fritz Oberhettinger, Raj Pal Soni, and Eugene P Wigner. Formulas and theorems for the special functions of mathematical physics. *Physics Today*, 20(12):81–83, 1967.

Shengbang Tong, Zhuang Liu, Yuexiang Zhai, Yi Ma, Yann LeCun, and Saining Xie. Eyes wide shut? exploring the visual shortcomings of multimodal llms. *2024 IEEE/CVF Conference on Computer Vision and Pattern Recognition (CVPR)*, pages 9568–9578, 2024. URL <https://api.semanticscholar.org/CorpusID:266976992>.

Can Yaras, Peng Wang, Wei Hu, Zhihui Zhu, Laura Balzano, and Qing Qu. The law of parsimony in gradient descent for learning deep linear networks. *arXiv preprint arXiv:2306.01154*, 2023.

Can Yaras, Peng Wang, Laura Balzano, and Qing Qu. Compressible dynamics in deep overparameterized low-rank learning & adaptation. In *Forty-first International Conference on Machine Learning*, 2024. URL <https://openreview.net/forum?id=uDkXoZMzBv>.

Soo Min Kwon, Zekai Zhang, Dogyoong Song, Laura Balzano, and Qing Qu. Efficient low-dimensional compression of overparameterized models. In *International Conference on Artificial Intelligence and Statistics*, pages 1009–1017. PMLR, 2024.

Xinlei Chen and Kaiming He. Exploring simple siamese representation learning. 2021 IEEE/CVF Conference on Computer Vision and Pattern Recognition (CVPR), pages 15745–15753, 2020. URL <https://api.semanticscholar.org/CorpusID:227118869>.

Kaiming He, Haoqi Fan, Yuxin Wu, Saining Xie, and Ross Girshick. Momentum contrast for unsupervised visual representation learning. In *Proceedings of the IEEE/CVF Conference on Computer Vision and Pattern Recognition*, pages 9726–9735, 2020. doi: 10.1109/CVPR42600.2020.00975.

Mathilde Caron, Ishan Misra, Julien Mairal, Priya Goyal, Piotr Bojanowski, and Armand Joulin. Unsupervised learning of visual features by contrasting cluster assignments. In *Advances in Neural Information Processing Systems*, NeurIPS’20, Red Hook, NY, USA, 2020. Curran Associates Inc. ISBN 9781713829546.

Christoph Feichtenhofer, Haoqi Fan, Bo Xiong, Ross Girshick, and Kaiming He. A large-scale study on unsupervised spatiotemporal representation learning. In *Proceedings of the IEEE/CVF Conference on Computer Vision and Pattern Recognition*, pages 3298–3308, 2021. doi: 10.1109/CVPR46437.2021.00331.

Siyi Chen, Minkyu Choi, Zesen Zhao, Kuan Han, Qing Qu, and Zhongming Liu. Unfolding videos dynamics via taylor expansion, 2024a. URL <https://arxiv.org/abs/2409.02371>.

Hongchao Fang and Pengtao Xie. CERT: contrastive self-supervised learning for language understanding. *CoRR*, abs/2005.12766, 2020. URL <https://arxiv.org/abs/2005.12766>.

Michael Heinzinger, Maria Littmann, Ian Sillitoe, Nicola Bordin, Christine Orengo, and Burkhard Rost. Contrastive learning on protein embeddings enlightens midnight zone. *NAR Genomics and Bioinformatics*, 4(2):lqac043, 06 2022. ISSN 2631-9268. doi: 10.1093/nargab/lqac043. URL <https://doi.org/10.1093/nargab/lqac043>.

Tongzhou Wang and Phillip Isola. Understanding contrastive representation learning through alignment and uniformity on the hypersphere. In *Proceedings of the 37th International Conference on Machine Learning*, ICML’20. JMLR.org, 2020.

Xianghong Fang, Jian Li, Xiangchu Feng, and Benyou Wang. Rethinking uniformity in self-supervised representation learning, 2023. URL <https://openreview.net/forum?id=hFULfiyf1oQ>.

Yihao Xue, Eric Gan, Jiayi Ni, Siddharth Joshi, and Baharan Mirzasoleiman. Investigating the benefits of projection head for representation learning. In *The Twelfth International Conference on Learning Representations*, 2024. URL <https://openreview.net/forum?id=GgEAdqYPNA>.

Kartik Gupta, Thalaiyasingam Ajanthan, Anton van den Hengel, and Stephen Gould. Understanding and improving the role of projection head in self-supervised learning, 2022. URL <https://arxiv.org/abs/2212.11491>.

Tianyu Hua, Wenxiao Wang, Zihui Xue, Yue Wang, Sucheng Ren, and Hang Zhao. On feature decorrelation in self-supervised learning. 2021 IEEE/CVF International Conference on Computer Vision (ICCV), pages 9578–9588, 2021. URL <https://api.semanticscholar.org/CorpusID:233481690>.

Sanjeev Arora, Hrishikesh Khandeparkar, Mikhail Khodak, Orestis Plevrakis, and Nikunj Saunshi. A theoretical analysis of contrastive unsupervised representation learning. In *International Conference on Machine Learning*, 2019. URL <https://api.semanticscholar.org/CorpusID:67855945>.

Chao Jia, Yinfei Yang, Ye Xia, Yi-Ting Chen, Zarana Parekh, Hieu Pham, Quoc V. Le, Yun-Hsuan Sung, Zhen Li, and Tom Duerig. Scaling up visual and vision-language representation learning with noisy text supervision. In Marina Meila and Tong Zhang, editors, *Proceedings of the 38th International Conference on Machine Learning, ICML 2021, 18-24 July 2021, Virtual Event*, volume 139 of *Proceedings of Machine Learning Research*, pages 4904–4916. PMLR, 2021. URL <http://proceedings.mlr.press/v139/jia21b.html>.

Richard Socher and Li Fei-Fei. Connecting modalities: Semi-supervised segmentation and annotation of images using unaligned text corpora. In *2010 IEEE Computer Society Conference on Computer Vision and Pattern Recognition*, pages 966–973, 2010. doi: 10.1109/CVPR.2010.5540112.

Yuhao Zhang, Hang Jiang, Yasuhide Miura, Christopher D. Manning, and C. Langlotz. Contrastive learning of medical visual representations from paired images and text. In *Machine Learning in Health Care*, 2020. URL <https://api.semanticscholar.org/CorpusID:222125307>.

Patrick Esser, Sumith Kulal, Andreas Blattmann, Rahim Entezari, Jonas Müller, Harry Saini, Yam Levi, Dominik Lorenz, Axel Sauer, Frederic Boesel, Dustin Podell, Tim Dockhorn, Zion English, and Robin Rombach. Scaling rectified flow transformers for high-resolution image synthesis. In *Forty-first International Conference on Machine Learning*, 2024. URL <https://openreview.net/forum?id=FPnUhsQJ5B>.

Simian Luo, Yiqin Tan, Longbo Huang, Jian Li, and Hang Zhao. Latent consistency models: Synthesizing high-resolution images with few-step inference. *ArXiv preprint arXiv:2310.04378*, 2023.

Chitwan Saharia, William Chan, Saurabh Saxena, Lala Li, Jay Whang, Emily L Denton, Kamyar Ghasemipour, Raphael Gontijo Lopes, Burcu Karagol Ayan, Tim Salimans, et al. Photorealistic text-to-image diffusion models with deep language understanding. *Advances in Neural Information Processing Systems*, 35:36479–36494, 2022b.

Maria A. Bravo, Sudhanshu Mittal, Simon Ging, and Thomas Brox. Open-vocabulary attribute detection. In *Proceedings of the IEEE/CVF Conference on Computer Vision and Pattern Recognition (CVPR)*, pages 7041–7050, June 2023.

Chenliang Zhou, Fangcheng Zhong, and Cengiz Öztireli. Clip-pae: Projection-augmentation embedding to extract relevant features for a disentangled, interpretable and controllable text-guided face manipulation. In *ACM SIGGRAPH 2023 Conference Proceedings, SIGGRAPH '23*, New York, NY, USA, 2023. Association for Computing Machinery. ISBN 9798400701597. doi: 10.1145/3588432.3591532. URL <https://doi.org/10.1145/3588432.3591532>.

Siyi Chen, Huijie Zhang, Minzhe Guo, Yifu Lu, Peng Wang, and Qing Qu. Exploring low-dimensional subspace in diffusion models for controllable image editing. In *The Thirty-eighth Annual Conference on Neural Information Processing Systems*, 2024b. URL <https://openreview.net/forum?id=50a0EfB2km>.

Changdae Oh, Junhyuk So, Hoyoon Byun, YongTaek Lim, Minchul Shin, Jong-June Jeon, and Kyungwoo Song. Geodesic multi-modal mixup for robust fine-tuning. In A. Oh,

T. Naumann, A. Globerson, K. Saenko, M. Hardt, and S. Levine, editors, *Advances in Neural Information Processing Systems*, volume 36, pages 52326–52341. Curran Associates, Inc., 2023. URL https://proceedings.neurips.cc/paper_files/paper/2023/file/a45296e83b19f656392e0130d9e53cb1-Paper-Conference.pdf.

Abrar Fahim, Alex Murphy, and Alona Fyshe. It’s not a modality gap: Characterizing and addressing the contrastive gap, 2024. URL <https://arxiv.org/abs/2405.18570>.

Sedigheh Eslami and Gerard de Melo. Mitigate the gap: Investigating approaches for improving cross-modal alignment in clip, 2024. URL <https://arxiv.org/abs/2406.17639>.

Joram Soch et al. Statproofbook/statproofbook.github.io: The book of statistical proofs (version 2023), 2024. URL <https://doi.org/10.5281/zenodo.4305949>.

DLMF. *NIST Digital Library of Mathematical Functions*. <https://dlmf.nist.gov/>, Release 1.2.2 of 2024-09-15. URL <https://dlmf.nist.gov/>. F. W. J. Olver, A. B. Olde Daalhuis, D. W. Lozier, B. I. Schneider, R. F. Boisvert, C. W. Clark, B. R. Miller, B. V. Saunders, H. S. Cohl, and M. A. McClain, eds.

Mehdi Cherti, Romain Beaumont, Ross Wightman, Mitchell Wortsman, Gabriel Ilharco, Cade Gordon, Christoph Schuhmann, Ludwig Schmidt, and Jenia Jitsev. Reproducible scaling laws for contrastive language-image learning. In *Proceedings of the IEEE/CVF Conference on Computer Vision and Pattern Recognition*, pages 2818–2829, 2023.

Kaiming He, X. Zhang, Shaoqing Ren, and Jian Sun. Deep residual learning for image recognition. *2016 IEEE Conference on Computer Vision and Pattern Recognition (CVPR)*, pages 770–778, 2015. URL <https://api.semanticscholar.org/CorpusID:206594692>.

Ashish Vaswani, Noam Shazeer, Niki Parmar, Jakob Uszkoreit, Llion Jones, Aidan N Gomez, Łukasz Kaiser, and Illia Polosukhin. Attention is all you need. In I. Guyon, U. Von Luxburg, S. Bengio, H. Wallach, R. Fergus, S. Vishwanathan, and R. Garnett, editors, *Advances in Neural Information Processing Systems*, volume 30. Curran Associates, Inc., 2017. URL https://proceedings.neurips.cc/paper_files/paper/2017/file/3f5ee243547dee91fdb053c1c4a845aa-Paper.pdf.

A Related Works

Contrastive Learning In the past, contrastive learning has been demonstrated as a powerful tool to learn reasonable representations in a self-supervised way (Chen and He, 2020; Chen et al., 2020; He et al., 2020; Caron et al., 2020). Representative contrastive methods including SimCLR (Chen et al., 2020), MOCO (He et al., 2020), and SwAV (Caron et al., 2020). Intuitively, contrastive learning aims to pair together data that contain similar information, and separate pairs that contain distinct information. Such a strategy can effectively extract key features within data that are useful for various downstream tasks. For example, by utilizing contrastive learning in images or videos, we can get image or video encoders that can perform zero-shot image and video retrieval, as well as image classification Chen et al. (2020); He et al. (2020); Caron et al. (2020), action detection, action segmantation, and other tasks (Feichtenhofer et al., 2021; Chen et al., 2024a). Moreover, contrastive learning can be applied to a wide range of data, from language to protein (Fang and Xie, 2020; Heinzinger et al., 2022). Apart from application, other works approach to analyze and understand contrastive learning from the perspective of alignment & uniformity (Wang and Isola, 2020; Fang et al., 2023), specific design choices (Xue et al., 2024; Gupta et al., 2022), and so on (Hua et al., 2021; Arora et al., 2019).

Multimodal Learning Multimodal learning aims to learn a shared representation space for different modalities such as images and texts, where the learned representation space can express the shared information hidden in different modalities (Jia et al., 2021; Radford et al., 2021; Socher and Fei-Fei, 2010). Under this context, contrastive learning has been proved applicable and powerful to multimodal learning (Radford et al., 2021). The contrastive loss is applied between two modalities (take image and text as an example) such that positive pairs (i.e., image and text pairs that contain similar information) have similar representations but negative pairs (i.e., image and text pairs that contain distinct information) are apart from each other. The pretrained multimodal models excel in various downstream tasks such as linear probe, zero-shot classification, and retrieval (Radford et al., 2021), and are even useful for medical applications (Zhang et al., 2020) and generative models (Esser et al., 2024; Luo et al., 2023; Saharia et al., 2022b). Despite its great power, recently, several works have also identified bias and flaws in the learned multimodal models, such as uni-model bias (Bravo et al., 2023), and failure in understanding detailed information (Tong et al., 2024), which add difficulty to applications such as text-to-image editing (Zhou et al., 2023; Chen et al., 2024b). Therefore, the theoretical understanding of contrastive multimodal learning is an important problem for further solving the aforementioned problems.

Modality Gap Following prior discoveries, existing works delve deeper into the modality gap from both theoretical and empirical perspectives. For instance, Shi et al. (2023) experimentally demonstrates the influence of different initialization and temperature parameters in the modality gap with toy datasets, but stops short of providing theoretical justifications for the emergence of modality gap under various conditions. Schrodi et al. (2024) investigates the role of information imbalance between modalities, suggesting that balancing information between text and image datasets helps close the modality gap. However, their claim is based solely on experiments with toy datasets and lacks a strong theoretical foundation. Instead of focusing on the reasons behind the modality gap, other studies propose practical solutions. For example, Oh et al. (2023) and Fahim et al. (2024) introduce new loss functions for fine-tuning the CLIP model to close the gap, while Eslami and de Melo (2024) encourages different modalities to share portions of their encoders. Although effective, they remain largely experimental and fail to provide a rigorous explanation for

modality gap's origin.

B Proofs

B.1 Preliminaries

The gradient of ℓ given in (2) is given by

$$\nabla \ell(\mathbf{M}) = \frac{1}{2n} \left(\frac{\exp(\mathbf{M})}{\mathbf{1}_n \mathbf{1}_n^\top \exp(\mathbf{M})} + \frac{\exp(\mathbf{M})}{\exp(\mathbf{M}) \mathbf{1}_n \mathbf{1}_n^\top} \right) - \frac{1}{n} \mathbf{I}_n$$

where division and exponentiation are carried out element-wise.

Define the function $g_a(\mathbf{Z}) := -\langle \mathbf{Z}, \nabla \ell(a\mathbf{Z}) \rangle$ which can be written as

$$g_a(\mathbf{Z}) = \frac{1}{2n} \left(\sum_{i=1}^n \mu_i(\mathbf{Z}_{:,i}, a) + \mu_i(\mathbf{Z}_{i,:}, a) \right)$$

where

$$\mu_i(\mathbf{z}, a) = \langle \mathbf{z}, \mathbf{e}^{(i)} - \sigma(a\mathbf{z}) \rangle \quad (10)$$

and σ is the softmax function $\sigma(\mathbf{m}) = \exp(\mathbf{m}) / \sum_j \exp(\mathbf{m}_j)$. Then we have

$$\frac{\partial \ell}{\partial \nu} = -\beta'(\nu)(1 - \gamma^2)g_{\beta(\nu)(1-\gamma^2)}(\mathbf{Z}), \quad \frac{\partial \ell}{\partial \gamma} = 2\beta(\nu)\gamma g_{\beta(\nu)(1-\gamma^2)}(\mathbf{Z})$$

which gives the gradient flow dynamics

$$\frac{d\beta}{dt} = (\beta')^2(1 - \gamma^2)g_{\beta(1-\gamma^2)}(\mathbf{Z}), \quad \frac{d\gamma}{dt} = -2\beta\gamma g_{\beta(1-\gamma^2)}(\mathbf{Z}) \quad (11)$$

where $\beta' := \beta'(\nu)$.

B.2 Proof of Lemma 3.1

Proof. From (11), we have

$$\frac{1}{2\beta\gamma} \left(-\frac{d\gamma}{dt} \right) = \frac{1}{(\beta')^2(1 - \gamma^2)} \frac{d\beta}{dt} \implies R = \frac{d\gamma/dt}{d\beta/dt} = -\frac{2\beta\gamma}{(\beta')^2(1 - \gamma^2)}$$

which gives (5). Now let $\beta = \exp(\nu)$ so $\beta' = \beta$. Then we can rewrite and integrate as

$$\int_{\beta_0}^{\beta} \frac{d\beta}{\beta} = -\frac{1}{2} \int_{\gamma_0}^{\gamma} \left(\frac{1}{\gamma} - \gamma \right) d\gamma \implies \beta(\gamma) = \beta_0 \sqrt{\frac{\gamma_0}{\gamma}} \exp\left(\frac{\gamma^2 - \gamma_0^2}{4}\right)$$

which gives (6). \square

B.3 Proof of Theorem 3.2

Lemma B.1. Let $\mathbf{z} \in \mathbb{R}^n$ and $i \in [n]$.

(a) If $\mathbf{z}_i \geq \max_j \mathbf{z}_j$, then $\mu_i(\mathbf{z}, a) \geq 0$ for all $a \geq 0$.

(b) For any $\alpha > 0$, we have

$$\mu_i(\mathbf{z}, a) \leq \mu_i(\alpha(\mathbf{e}^{(i)} - \mathbf{1}), a)$$

for all $a \geq \log(4n-4)/\alpha$ and for all \mathbf{z} such that $\mathbf{z}_i - \max_{j \neq i} \mathbf{z}_j \geq \alpha$.

Proof. We have

$$\langle \mathbf{z}, \mathbf{e}^{(i)} \rangle = \mathbf{z}_i \geq \max_j \mathbf{z}_j = \sum_l \sigma_l(a\mathbf{z}) \left(\max_j \mathbf{z}_j \right) \geq \sum_l \sigma_l(a\mathbf{z}) \mathbf{z}_l = \langle \mathbf{z}, \sigma(a\mathbf{z}) \rangle$$

so $\mu_i(\mathbf{z}, a) \geq 0$, giving (a).

To prove (b), without loss of generality, we can take $i = 1$ and assume $\mathbf{z}_1 = 0$ and $\mathbf{z}_j \leq -\alpha$ for $j \neq 1$. Define $\mathbf{w} = \mathbf{z}_{2:n} \in \mathbb{R}^{n-1}$ and

$$\psi(\mathbf{w}, a) := \frac{\sum_j \mathbf{w}_j \exp(a\mathbf{w}_j)}{1 + \sum_j \exp(a\mathbf{w}_j)}$$

so that $\mu_1(\mathbf{z}, a) = -\psi(\mathbf{w}, a)$. The statement is then equivalent to showing $\psi(\mathbf{w}, a) \geq \psi(-\alpha\mathbf{1}, a)$ for any \mathbf{w} such that $\mathbf{w}_j \leq -\alpha$ for all $j \in [n-1]$. It suffices to show that for any k , we have $\partial\psi/\partial\mathbf{w}_k \leq 0$ whenever $\mathbf{w} \preceq -\alpha\mathbf{1}$, i.e., ψ is decreasing in any argument for the region bounded above by $-\alpha\mathbf{1}$. We compute

$$\frac{\partial\psi}{\partial\mathbf{w}_k} = \frac{\exp(a\mathbf{w}_k)}{1 + \sum_j \exp(a\mathbf{w}_j)} (1 + a\mathbf{w}_k - a\psi(\mathbf{w}, a))$$

where

$$a\psi(\mathbf{w}, a) = \frac{\sum_j a\mathbf{w}_j \exp(a\mathbf{w}_j)}{1 + \sum_j \exp(a\mathbf{w}_j)} \geq \sum_j a\mathbf{w}_j \exp(a\mathbf{w}_j) \geq -(n-1)a\alpha \exp(-a\alpha)$$

provided that $\mathbf{w} \preceq -\alpha\mathbf{1}$, where the last inequality follows from $\alpha \geq 1/a$. Now, for any $x \geq \log(4n-4)$, we have that $(n-1) \leq \exp(x)(1-1/x)$ by $1-1/x \geq 1/4$. Therefore, $x = a\alpha \geq \log(4n-4)$ satisfies

$$(n-1) \exp(-a\alpha) \leq 1 - \frac{1}{a\alpha} \implies -(n-1)a\alpha \exp(-a\alpha) \geq 1 - a\alpha.$$

Combining the above inequalities along with $1 + a\mathbf{w}_k \leq 1 - a\alpha$ yields $a\psi(\mathbf{w}, a) \geq 1 + a\mathbf{w}_k$, and thus $\partial\psi/\partial\mathbf{w}_k \leq 0$, completing the proof. \square

Proof of Theorem 3.2. First, we note by (11) that $\beta(t)$ is increasing in t and $\gamma(t)$ is decreasing in t due to the fact that $g_{\beta(1-\gamma^2)}(\mathbf{Z}) \geq 0$ via perfect mismatch and (a) in Lemma B.1. Now, we can substitute the expression for β in (6) into the dynamics of γ in (11) giving

$$\frac{d\gamma}{dt} = -2\beta(\gamma)\gamma g_{\beta(\gamma)(1-\gamma^2)}(\mathbf{Z}).$$

Since

$$\beta(\gamma)(1 - \gamma^2) \geq \beta_0 \exp(-\gamma_0^2/4)(1 - \gamma_0^2)$$

we have by $\beta_0 \geq \log(4n - 4)/(\bar{\alpha}(1 - \gamma_0^2))$, (b) in Lemma B.1, and the fact that $\beta(t)$ and $\gamma(t)$ are increasing and decreasing in t respectively that

$$\begin{aligned} g_{\beta(\gamma)(1-\gamma^2)}(\mathbf{Z}) &\leq \mu_1 \left(\bar{\alpha}(\mathbf{e}^{(1)} - \mathbf{1}), \beta(\gamma)(1 - \gamma^2) \right) \\ &= 1 - (p_1 + (1 - \bar{\alpha})(1 - p_1)) = \bar{\alpha}(1 - p_1) \end{aligned}$$

where p_1 is the first entry of $\sigma(\beta(\gamma)(1 - \gamma^2)\bar{\alpha}(\mathbf{e}^{(1)} - \mathbf{1}))$. We compute

$$1 - p_1 = \frac{1}{1 + \exp(\beta(\gamma)(1 - \gamma^2)\bar{\alpha})/(n - 1)} \leq (n - 1) \exp(-\beta(\gamma)(1 - \gamma^2)\bar{\alpha})$$

so overall we have

$$\begin{aligned} 2\beta(\gamma)\gamma g_{\beta(1-\gamma^2)}(\mathbf{Z}) &\leq 2\bar{\alpha}(n - 1)\beta(\gamma)\gamma \exp(-\beta(\gamma)(1 - \gamma^2)\bar{\alpha}) \\ &\leq 2\bar{\alpha}(n - 1)\beta_0 \sqrt{\frac{\gamma_0}{\gamma}} \gamma \exp\left(-\beta_0 \sqrt{\frac{\gamma_0}{\gamma}} \exp\left(-\frac{\gamma_0^2}{4}\right) (1 - \gamma_0^2)\bar{\alpha}\right) \end{aligned}$$

where the second inequality follows from $\gamma \leq \gamma_0$ and $\exp(-\gamma_0^2/4) \leq \exp((\gamma^2 - \gamma_0^2)/4) \leq 1$. Let $c_1 = 2\bar{\alpha}(n - 1)\beta_0 \sqrt{\gamma_0}$ and $c_2 = \bar{\alpha}\beta_0 \sqrt{\gamma_0}(1 - \gamma_0^2) \exp(-\gamma_0^2/4)$, and define a new problem

$$\frac{d\tilde{\gamma}}{dt} = -c_1 \sqrt{\tilde{\gamma}} \exp\left(-\frac{c_2}{\sqrt{\tilde{\gamma}}}\right)$$

with initial condition $\tilde{\gamma}(0) = \gamma_0$. Since $d\tilde{\gamma}/dt \leq d\gamma/dt$ whenever $\tilde{\gamma} = \gamma$, we have that $\tilde{\gamma}(t) \leq \gamma(t)$ for all $t \geq 0$. We make the change of variables $\omega = 1/\sqrt{\tilde{\gamma}}$ which gives

$$\frac{d\omega}{dt} = (1/2)c_1\omega^2 \exp(-c_2\omega)$$

with $\omega(0) = 1/\sqrt{\gamma_0}$. From the fact that $(1/55)x^2 \exp(-x/10) \leq 1$ for all $x \geq 0$, we have that

$$(1/2)c_1\omega^2 \exp(-c_2\omega) \leq c_3 \exp(-c_4\omega)$$

where $c_3 = 55c_1/2$ and $c_4 = c_2 - 1/10$ so defining

$$\frac{d\tilde{\omega}}{dt} = c_3 \exp(-c_4\tilde{\omega})$$

with $\tilde{\omega}(0) = \omega(0) = 1/\sqrt{\gamma_0}$ satisfies $\tilde{\omega}(t) \geq \omega(t)$ for all $t \geq 0$. Integrating, we have $\tilde{\omega}(t) = (1/c_4) \log(c_3 t + \exp(c_4/\sqrt{\gamma_0}))$, and combining all the above bounds yields

$$\gamma(t) \geq \frac{c_2}{\log(c_3 t + \exp(c_4/\sqrt{\gamma_0}))^2}$$

for all $t \geq 0$, which combined with $\Delta \geq 2\gamma$ completes the proof. \square

B.4 Proof of Theorem 3.3

Lemma B.2. Let $\mathbf{x}, \mathbf{y} \stackrel{iid}{\sim} \text{Uniform}(\mathbb{S}^{d-1})$. Then $z = \langle \mathbf{x}, \mathbf{y} \rangle \sim f_Z$ where

$$f_Z(z) = \Gamma(d/2)/(\sqrt{\pi} \Gamma((d-1)/2)) (1-z^2)^{(d-3)/2}, \quad z \in [-1, 1]. \quad (12)$$

Proof. By symmetry, we can fix $\mathbf{y} = \mathbf{e}^{(1)}$. We have that $z^2 = x_1^2 \stackrel{d}{=} w_1^2/(w_1^2 + \dots + w_d^2)$ where $w_1, \dots, w_d \stackrel{iid}{\sim} \mathcal{N}(0, 1)$. Letting $v_1 = w_1^2$ and $v_2 = w_2^2 + \dots + w_d^2$ such that $v_1 \sim \chi_1^2$ and $v_2 \sim \chi_{d-1}^2$, we have $z^2 = v_1/(v_1 + v_2) \sim \text{Beta}(1/2, (d-1)/2)$ (see the relationship between chi-squared distribution and beta distribution in Soch et al. (2024)). Then we have

$$F_{Z^2}(z^2) = \mathbb{P}\{Z^2 \leq z^2\} = \mathbb{P}\{-z \leq Z \leq z\} = 2F_Z(z)$$

hence

$$\begin{aligned} f_Z(z) = z f_{Z^2}(z^2) &= \frac{\Gamma(d/2)}{\Gamma(1/2)\Gamma((d-1)/2)} z \cdot z^{2(1/2-1)} (1-z^2)^{(d-1)/2-1} \\ &= \frac{\Gamma(d/2)}{\sqrt{\pi} \Gamma((d-1)/2)} (1-z^2)^{(d-3)/2}, \end{aligned}$$

completing the proof. \square

Lemma B.3. Let $z \sim f_Z$ where f_Z is given in (12) and $a > 0$. Then we have $\mathbb{E}[z] = 0$, and

$$\mathbb{E}[\exp(az)] = \Gamma\left(\frac{d}{2}\right) \left(\frac{2}{a}\right)^\rho I_\rho(a) \quad (13)$$

$$\mathbb{E}[z \exp(az)] = \Gamma\left(\frac{d}{2}\right) \left(\frac{2}{a}\right)^\rho \left(I_{\rho-1}(a) - \frac{2\rho}{a} I_\rho(a) \right) \quad (14)$$

where $\rho = (d-2)/2$, Γ is the gamma function and $I_\rho(z)$ is the modified Bessel function of the first kind.

Proof. The first claim $\mathbb{E}[z] = 0$ follows directly from symmetry of f_Z . Now define

$$F(a, d) = \frac{1}{\sqrt{\pi} \Gamma((d-1)/2)} \int_{-1}^1 \exp(az) (1-z^2)^{(d-3)/2} dz.$$

From the identity in (DLMF, (10.32.2)), we have that $F(a, d) = (2/a)^{(d-2)/2} I_{(d-2)/2}$. Now

$$\mathbb{E}[\exp(az)] = \frac{\Gamma(d/2)}{\sqrt{\pi} \Gamma((d-1)/2)} \int_{-1}^1 \exp(az) (1-z^2)^{(d-3)/2} dz = \Gamma(d/2) F(a, d)$$

which gives (13). On the other hand, we have

$$\mathbb{E}[z \exp(az)] = \frac{d \mathbb{E}[\exp(az)]}{da} = \Gamma(d/2) \frac{dF(a, d)}{da}$$

where

$$\frac{dF(a, d)}{da} = \frac{1}{2} (1-d/2) \left(\frac{2}{a}\right)^{d/2} I_{(d-2)/2}(a) + \left(\frac{2}{a}\right)^{(d-2)/2} \frac{dI_{(d-2)/2}(a)}{da}$$

with

$$\frac{dI_{(d-2)/2}(a)}{da} = I_{(d-4)/2} - \frac{(d-2)}{2a} I_{(d-2)/2}(a)$$

by the identity in (Magnus et al., 1967, (3.1.1)). Putting together the above formulas and simplifying yields (14), completing the proof. \square

Proof of Theorem 3.3. Let $\mathbf{Z} = \mathbf{H}_X(0)\mathbf{H}_Y^\top(0)$, so by Lemma B.2 we have $\mathbf{Z}_{ij} \sim f_Z$ where f_Z is given by (12). We also note that any given row, column, or diagonal of \mathbf{Z} forms a collection of independent variables (but not the entire matrix).

Let $\mathbf{z} \in [-1, 1]^n$ be a given row, column, or the diagonal of \mathbf{Z} . From Lemma B.3 we have $\mathbb{E}[\mathbf{z}] = 0$, and let $\xi_1 = \mathbb{E}[\mathbf{z} \exp(a\mathbf{z})]$ and $\xi_2 = \mathbb{E}[\exp(a\mathbf{z})]$. By $\mathbf{z}_i \in [-1, 1]$, $\mathbf{z}_i \exp(a\mathbf{z}_i) \in [-e^a, e^a]$, and $\exp(a\mathbf{z}_i) \in [e^{-a}, e^a]$ for all $i \in [n]$, applying one-sided Hoeffding inequalities gives

$$\begin{aligned} \mathbb{P} \left\{ \frac{1}{n} \sum_j \mathbf{z}_j \leq 2\sqrt{\frac{\log(1/\delta)}{2n}} \right\} &\geq 1 - \delta, \\ \mathbb{P} \left\{ \frac{1}{n} \sum_j \mathbf{z}_j \exp(a\mathbf{z}_j) \geq \xi_1 - 2e^a \sqrt{\frac{\log(1/\delta)}{2n}} \right\} &\geq 1 - \delta, \\ \mathbb{P} \left\{ \frac{1}{n} \sum_j \exp(a\mathbf{z}_j) \leq \xi_2 + (e^a - e^{-a}) \sqrt{\frac{\log(1/\delta)}{2n}} \right\} &\geq 1 - \delta. \end{aligned}$$

Let $a_0 = \beta_0(1 - \gamma_0^2)$. We compute

$$\begin{aligned} \frac{d\gamma}{dt} \Big|_{t=0} &= -2\beta_0\gamma_0 g_{\beta_0(1-\gamma_0^2)}(\mathbf{Z}) \\ &= -\frac{\beta_0\gamma_0}{n} \left(\sum_{i=1}^n \mu_i(\mathbf{Z}_{:,i}, a_0) + \mu_i(\mathbf{Z}_{i,:}, a_0) \right) \\ &= -\frac{\beta_0\gamma_0}{n} \left(\sum_{i=1}^n \langle \mathbf{Z}_{:,i}, \mathbf{e}^{(i)} - \sigma(a_0 \mathbf{Z}_{:,i}) \rangle + \langle \mathbf{Z}_{i,:}, \mathbf{e}^{(i)} - \sigma(a_0 \mathbf{Z}_{i,:}) \rangle \right) \\ &= \frac{\beta_0\gamma_0}{n} \left(\sum_{i=1}^n \langle \mathbf{Z}_{:,i}, \sigma(a_0 \mathbf{Z}_{:,i}) \rangle + \sum_{i=1}^n \langle \mathbf{Z}_{i,:}, \sigma(a_0 \mathbf{Z}_{i,:}) \rangle - 2 \sum_{j=1}^n \mathbf{Z}_{j,j} \right) \\ &= \frac{\beta_0\gamma_0}{n} \left(\sum_{i=1}^n \frac{\frac{1}{n} \sum_{j=1}^n \mathbf{Z}_{j,i} \exp(a_0 \mathbf{Z}_{j,i})}{\frac{1}{n} \sum_{j=1}^n \exp(a_0 \mathbf{Z}_{j,i})} + \sum_{i=1}^n \frac{\frac{1}{n} \sum_{j=1}^n \mathbf{Z}_{i,j} \exp(a_0 \mathbf{Z}_{i,j})}{\frac{1}{n} \sum_{j=1}^n \exp(a_0 \mathbf{Z}_{i,j})} - 2 \sum_{j=1}^n \mathbf{Z}_{j,j} \right). \end{aligned}$$

Applying the above concentration inequalities yields

$$\frac{d\gamma}{dt} \Big|_{t=0} \geq 2\beta_0\gamma_0 \left(\frac{\xi_1 - 2e^{a_0}\epsilon}{\xi_2 + (e^{a_0} - e^{-a_0})\epsilon} - 2\epsilon \right)$$

with probability $1 - \delta$ where $\epsilon = \sqrt{\log((4n+1)/\delta)/(2n)}$ by union bound for $4n+1$ events. Finally, we have $d\Delta/dt \geq 2d\gamma/dt$ by $\Delta \geq 2\gamma$ which gives the result. \square

C Alternate Temperature Schemes

Consider the simplified setting $\ell(m) = \exp(-m)$ discussed in Section 3.

Temperature reparameterization. Take $\beta(\nu) = \nu$ with $\beta'(\nu) = 1$ for $\nu > 0$. Integrating (5) gives $\beta(\gamma) = \Theta(\log(1/\gamma)^{1/2})$, which grows significantly slower compared to (6) as $\gamma \rightarrow 0$. As a result, the dynamics of γ become $d\gamma/dt = \Theta(-\log(1/\gamma)^{1/2}\gamma \exp(-\log(1/\gamma)^{1/2}))$, which has solution $\gamma(t) = \Theta(1/t^{\log(t)})$, a significantly *faster* rate of convergence than the one in Theorem 3.2.

Temperature scheduling. Alternatively, one can consider a temperature *schedule*, where $\beta(t)$ is simply a function of time t . Then $\gamma(t) = \Theta\left(\exp\left(-\int_0^t \beta(s) \exp(-\beta(s)) ds\right)\right)$. In the simplest case, we can consider $\beta(s) = \beta_0$, i.e., a constant temperature, for which we have $\gamma(t) = \Theta(\exp(-\beta_0 \exp(-\beta_0)t))$. Provided that β_0 is not too large or too small, the modality gap closes quickly at a linear rate. More generally, a linear schedule $\beta(s) = (1 - (s/t))\beta_0 + (s/t)\beta_1$ also yields a linear decay $\gamma(t) = \exp(-c(\beta_0, \beta_1)t)$ where $c(\beta_0, \beta_1) = [(\beta_0 + 1)\exp(-\beta_0) - (\beta_1 + 1)\exp(-\beta_1)]/(\beta_1 - \beta_0)$, while allowing a sweep of temperature values throughout training.

D Methods

In this section, we introduce the proposed methods in greater details, and present representative results in Table 2 as examples. We include more ablation studies in Appendix F.

D.1 Temperature Control

Temperature Scheduling (TS). First, we propose to not learn the temperature as (Radford et al., 2021). Instead, we schedule the increase of temperature according to the training epochs *linearly*. With a larger temperature in the late stage, we can make more progress on reducing the modality gap. As shown in Table 2, linearly increasing temperature from 10^{-2} to $5 \cdot 10^{-2}$ over the training process reduces the modality gap and leads to better text-image retrieval performance.

Temperature Reparameterization (TR). Towards the same purpose, TR designs different parameterization $\tau(\nu)$ from CLIP to slow down the decreasing of $\tau(\nu)$ when learning ν . In comparison with the original CLIP with $1/\tau(\nu) = \exp(\nu)$, we propose to use $1/\tau(\nu) = \exp(\nu/s)$ with $s > 1$ being a scalar to reduce the influence of ν as it grows. Another way we propose is to design through softplus to achieve the same goal: $1/\tau(\nu) = \log(1 + e^\nu)$. We report results using softplus in Table 2.

Smaller Learning Rate of Temperature (SLRT). To slow down the decrease of $\tau(\nu)$, SLRT scales down the learning rate of ν directly. In Table 2, we report the results from scaling the learning rate of ν by 10^{-1} . The result shows improved performance with reduced gap. It implies that the original choice of ν in CLIP is far from optimal, and can be improved through a careful analysis.

Fixed on Large Temperature (FLT). FLT freezes the temperature instead of learning it. We let $\tau(\nu)$ range from 10^{-2} to $4 \cdot 10^{-1}$ to find temperatures that can shrink the modality gap. The results from Table 2 is obtained with $\tau(\nu) = 4 \cdot 10^{-2}$.

D.2 Swap Modalities

Hard Swapping Between Modalities (HS). Recall $\mathbf{H}_X, \mathbf{H}_Y \in \mathbb{R}^{n \times d}$ denote the image and text features. HS randomly swaps $\mathbf{H}_X[i, j]$ and $\mathbf{H}_Y[i, j]$ for each (i, j) independently with probability 0.5 to obtain $\bar{\mathbf{H}}_X, \bar{\mathbf{H}}_Y$. Then, the swapped features are input to the loss function for optimizing networks.

	Baseline	Controlling the Temperature				Eliminating the Separation of Modalities	
		FLT	TS	TR	SLRT	HS	SS
Modality Gap (↓)	0.294	0.122	0.088	0.284	0.268	0.225	0.139
Uniformity (↑)	-1.165	-1.183	-1.108	-1.153	-1.152	-1.156	-1.152
Zero-shot (↑)	13.650	14.400	17.167	14.860	15.130	13.910	14.330
Linear Probe (↑)	65.550	61.980	67.500	66.460	66.630	65.950	64.940
Image Retrieval (↑)	68.233	73.440	75.723	70.060	70.320	69.716	68.912
Text Retrieval (↑)	78.367	82.660	85.313	80.100	80.400	79.740	79.160

Table 2: **Mitigating the modality gap with our proposed methods.**

Such swapping only happens for p random portion of the training, thus p controls how much swapping is applied across training. We have conducted search on p from $1e-3$ to 1.0 . It turns out to be a strong method for closing the gap. The results from Table 2 are obtained with $p = 1e-3$.

Soft Swapping Between Modalities (SS). SS is similar to HS, but swaps entries in a soft way. In SS, we randomly sample $\lambda_{ij} \in [0, 1]$ for each (i, j) independently, and then set $\bar{\mathbf{H}}_X[i, j] = \lambda_{ij} \mathbf{H}_X[i, j] + (1 - \lambda_{ij}) \mathbf{H}_Y[i, j]$ and $\bar{\mathbf{H}}_Y[i, j] = \lambda_{ij} \mathbf{H}_Y[i, j] + (1 - \lambda_{ij}) \mathbf{H}_X[i, j]$. Similarly, the swapped features are input to the loss function for optimizing networks. Besides, swapping is also conducted for p random portion of the training. We have conducted a search on p from $1e-2$ to $1e-1$. The result from Table 2 is obtained with $p = 5e-2$.

E Experiment Settings

E.1 Pretraining

Basics For the CLIP pretraining on MSCOCO using the train split, we utilize the OpenCLIP platform produced by Cherti et al. (2023). The neural network architecture for the image encoder is ResNet-50 (He et al., 2015) and the architecture for the text encoder is Transformer (Vaswani et al., 2017). Both architectures can be specified by ‘RN50’ in the OpenCLIP platform. The input image is RandomResizedCrop to 224×224 followed by Normalization. For each method of pretraining, we select the best learning rate from $[1e-5, 5e-5, 1e-4, 5e-4]$. For each training process, we train the model for 100 epochs with batchsize 1024 using a cosine decay learning rate schedule and 20 warmup epochs. We conduct the training 3 times for each specific setting and report the mean of the results among all 3 trainings.

Computing Requirements All the experiments can be conducted on a single A100 GPU.

E.2 Metrics

Modality Gap We measure the modality gap as modality center distance. The center distance is calculated between 512 random pairs in the MSCOCO test split. Let \mathbf{X} and \mathbf{Y} be image and text features, where each column is a feature sample, we define the modality centers as

$$\mathbf{c}_X = \frac{1}{n} \sum_{j=1}^n \mathbf{x}_j, \mathbf{c}_Y = \frac{1}{n} \sum_{j=1}^n \mathbf{x}_j.$$

Then as proposed in Liang et al. (2022), we measure modality gap by the center distance:

$$m_{XY} = \|\Delta\| = \|\mathbf{c}_X - \mathbf{c}_Y\|.$$

The center distance reported is also averaged among three independent trainings. A larger center distance indicates a larger modality gap.

Uniformity We utilize the uniformity metric proposed by Fang et al. (2023). After concatenating \mathbf{X} and \mathbf{Y} and obtain $\mathbf{Z} \in \mathbb{R}^{d \times 2n}$, we define the sample mean of \mathbf{Z} as $\hat{\mu}$ and the sample variance of \mathbf{Z} as $\hat{\Sigma}$. Calculate the quadratic Wasserstein distance between $\mathcal{N}(\hat{\mu}, \hat{\Sigma})$ and $\mathcal{N}(\mathbf{0}, \mathbf{I}/m)$:

$$\mathcal{W}_2 := \sqrt{\|\hat{\mu}\|_2^2 + 1 + \text{tr}(\hat{\Sigma}) - \frac{2}{\sqrt{m}} \text{tr}(\hat{\Sigma}^{\frac{1}{2}})}.$$

Then $-\mathcal{W}_2$ serves as the uniformity metric. A larger value of $-\mathcal{W}_2$ indicates a better uniformity of the feature space spanned by \mathbf{Z} .

E.3 Downstream Tasks

Linear Probe We conduct linear probing on CIFAR 10 following the same setting in Radford et al. (2021). After pertaining, we extract the image features from the vision encoder, and train a logistic regression based using the features in the train split. We evaluate the classification accuracy of the features in the test split and report the averaged results across three independent trainings. We report the Top-1 classification accuracy.

Zero-shot Classification We conduct linear probing on CIFAR 10 following the same setting in Radford et al. (2021). For each class containing [NUMBER], we construct the text prompt as "A photo of the number [NUMBER]". For each image, the text encoder will embed the text prompts into text features for all classes, and the image encoder will embed the image into an image feature. The probability of each class is then obtained from the softmax of the cosine similarities between the text features and the image feature scaled by temperature. We report the Top-1 classification accuracy. All values are averaged across three trainings.

Text-image Retrieval We conduct image-to-text retrieval and text-to-image retrieval on the text split of MSCOCO, and report the Top-1 recall. All values are averaged across three trainings. Image-to-text retrieval aims to retrieve the most relevant text description given an input image by computing the similarities of image and text features, while text-to-image retrieval is performed the other way around.

MMVP-VLM The MMVP-VLM benchmark is proposed by Tong et al. (2024), which can be viewed as a "difficult retrieval task". Given two image and text pairs $(\mathbf{x}_1, \mathbf{y}_1)$ and $(\mathbf{x}_2, \mathbf{y}_2)$ that only have differences concerning certain detailed visual pattern, the CLIP model is required to perfectly match the two pairs. They define 9 visual patterns: Orientation and Direction, Presence of Specific Features, State and Condition, Quantity and Count, Positional and Relational Context, Color and Appearance, Structural and Physical Characteristics, Text, and Viewpoint and Perspective. Each visual pattern contains several text-image pairs for constructing the matching task. We report the average accuracy across 9 visual pattern groups. All results are averaged across three trainings.

	Uniformity	Modality Gap	Zero Shot	Linear Probe	Image Retrieval	Text Retrieval
Baseline	-1.165	0.294	13.65	65.55	68.23	78.36
1.00E-02	-1.214	0.669	18.48	69.44	69.89	80.68
2.00E-02	-1.138	0.334	18.83	68.41	70.54	81.3
4.00E-02	-1.183	0.122	14.4	61.98	73.44	82.66
7.00E-02	-1.246	0.033	11.76	49.61	75.53	82.88
1.00E-01	-1.251	0.019	10.42	48.29	66.55	73.58
2.00E-01	-1.255	0.008	10.55	50.14	23.97	26.94
3.00E-01	-1.282	0.007	10.69	42.09	10.4	12.8
4.00E-01	-1.296	0.009	13.83	37.97	6.9	8.7

Table 3: **More results for fixed temperature (FLT).**

	Uniformity	Modality Gap	Zero Shot	Linear Probe	Image Retrieval	Text Retrieval
Baseline	-1.165	0.294	13.65	65.55	68.23	78.36
S0	-1.120	0.384	18.40	69.40	72.55	82.89
S1	-1.087	0.198	18.55	69.26	72.69	83.05
S2	-1.092	0.137	16.80	68.25	73.98	84.25
S3	-1.108	0.088	17.17	67.50	75.72	85.31
A0	-1.151	0.541	19.50	69.47	72.51	81.97
A1	-1.120	0.261	16.85	67.46	73.90	83.65

Table 4: **More results for temperature scheduling (TS).**

F Additional Experimental Results

In this section, we provide more detailed results on different methods that reduce (or enlarge) the modality gap. We introduce details of the results below.

- More results for fixed temperature: we provide a more fine-grid temperature search from $1e^{-2}$ to $4e^{-1}$, and present the results in Table 3.
- More results for temperature scheduling: The three temperature schedules S1, S2, S3 presented in Table 1 in Section 4.1 have the following schedules. S1 corresponds to linearly increasing temperature from $1e-2$ to $3e-2$, S2 corresponds to linearly increasing temperature from $1e-2$ to $4e-2$, and S3 corresponds to linearly increasing temperature from $1e-2$ to $5e-2$. Apart from the above scheduling, we additionally show results for S1, A0, and A1 in Table 4. Here, S0 corresponds to linearly increasing temperature from $1e-2$ to $2e-2$, A1 corresponds to the alternation of temperature between $1e-2$ and $2e-2$, and A2 corresponds to the alternation of temperature between $1e-2$ and $4e-2$. Temperature alternation follows a cosine function.
- More results for other methods: More results for other methods are shown in Table 5. Here, Scale2 and Scale10 corresponding to temperature parameterization with $\tau(\nu) = \exp(\frac{\nu}{s})$, where $s = 2, 10$, respectively. HS P* refers to Hard Swapping with $p = *$ as discussed in Appendix D. Besides, Hard Swap Feature means swapping the entire row instead of independent entries. It can also break the modality boundary but with greater constraints. As

	Uniformity	Modality Gap	Zero Shot	Linear Probe	Image Retrieval	Text Retrieval
Baseline	-1.165	0.294	13.65	65.55	68.23	78.36
Softplus	-1.153	0.284	14.86	66.46	70.06	80.1
Scale2	-1.154	0.287	18.25	66.3	70.32	80.6
Scale10	-1.153	0.285	14.36	66.5	70.15	80.3
HS P1	-1.317	0.028	14.36	39.72	47.17	53.22
HS P1e-1	-1.127	0.046	17.39	56.88	67.1	75.8
HS P1e-2	-1.181	0.095	15.7	64.29	69.36	79.4
Hard Swap Feature	-1.155	0.289	14.71	65.91	69.93	80.6
Remove Normalization	-1.005	0.468	16.82	65.4	58.62	74.16

Table 5: **More results for other methods.**

we can see, Hard Swap Feature reduces the center distance as well, but the reduced amount is less than HS (swapping entries). Lastly, Remove Normalization means freezing the temperature while removing the normalization of features during training. This approach is equivalent to learning a "temperature parameter" for each feature, in the sense that the temperature parameter is a global scaling of feature norms. With more freedom in changing the "temperatures" to optimize losses, Remove Normalization results in a larger modality gap.